

# Laser Pulsing in Linear Compton Scattering

G. A. Krafft<sup>1,2</sup>, E. Johnson<sup>1</sup>, K. Deitrick<sup>1</sup>, B. Terzić<sup>1</sup>, R. Kelmar<sup>3</sup>, T. Hodges<sup>4</sup>, W. Melnitchouk<sup>2</sup>, J. R. Delayen<sup>1,2</sup>

<sup>1</sup>*Department of Physics, Center for Accelerator Science,  
Old Dominion University, Norfolk, Virginia 23529*

<sup>2</sup>*Thomas Jefferson National Accelerator Facility, Newport News, Virginia 23606*

<sup>3</sup>*Department of Physics, Union College, Schenectady, New York 12308*

<sup>4</sup>*Department of Physics, Arizona State University, Tempe, Arizona 85004*

Previous work on calculating energy spectra from Compton scattering events has either neglected considering the pulsed structure of the incident laser beam, or has calculated these effects in an approximate way subject to criticism. In this paper, this problem has been reconsidered within a linear plane wave model for the incident laser beam. By performing the proper Lorentz transformation of the Klein-Nishina scattering cross section, a spectrum calculation can be created which allows the electron beam energy spread and emittance effects on the spectrum to be accurately calculated, essentially by summing over the emission of each individual electron. Such an approach has the obvious advantage that it is easily integrated with a particle distribution generated by particle tracking, allowing precise calculations of spectra for realistic particle distributions “in collision”. The method is used to predict the energy spectrum of radiation passing through an aperture for the proposed Old Dominion University inverse Compton source. Many of the results allow easy scaling estimates to be made of the expected spectrum.

PACS numbers: 29.20.Ej, 29.25.Bx, 29.27.Bd, 07.85.Fv

## I. INTRODUCTION

Compton or Thomson scattering can be used in constructing sources of high energy photons [1–4]. In recent years there has been a revival of activity in the subject driven by the desire to produce several keV X-ray sources from relatively compact relativistic electron accelerators. Such sources are attractive due to the narrow bandwidth generated in the output radiation. A group at Old Dominion University (ODU) and Jefferson Lab has been actively engaged in designing such a source [5, 6]. As part of the design process, it is important to quantify the effect of electron beam energy spread, electron beam emittance, and the finite laser pulse length on the radiation generated. In the course of our design process we have developed a calculation method yielding the energy spectral distribution of the radiation produced by the scattering event, and extended it so that the radiation from a bunch of relativistic electrons may be obtained. In this paper we summarize the calculation method, and use it in a benchmarking calculation to confirm several results previously published [7]. In addition, we use the method to suggest a needed correction in Ref. [8], and to make predictions regarding X-ray source performance for a compact Superconducting RF (SRF) linac based source proposed at ODU. The calculations show that the expected brilliance from this source will be world-leading for Compton sources.

Our calculation method is somewhat different from others [9, 10] because the incident laser electromagnetic field is specified as an input to the calculation through the normalized vector potential. Thus the finite pulse effects possible in a real laser pulse will be modeled properly within a plane-wave approximation. The flat-pulse approximation is not adopted [11], although this case can be encompassed within the method. Likewise, it is not necessary to characterize the incident photon beam only by a series of moments. More flexibility is allowed through investigating various models for the vector potential. The approach in this calculation is closest to that of Petrillo *et al.* [12]. We note, however, that some modifications of their published calculations are needed. On the other hand, we confirm their results, with some exceptions noted, by also calculating with parameters for the Extreme Light Infrastructure (ELI) - Nuclear Physics [13].

We report on calculations completed using the quantum mechanical Klein-Nishina [14] cross section (higher order quantum effects are neglected) under the assumption that the incident laser field is a plane wave. The number density of incident photons is related to the wave function of the incident field using the usual semiclassical approach. As such, this approximation is invalid in situations with highest field strengths where multiphoton quantum emission can occur. In contrast to our previous work on this subject [15] the full Compton recoil is included, from which the linear Thomson scattering results are recovered properly.

As a result of our design work, a literature search concerning the scattering of circularly polarized laser beams was undertaken. Perhaps surprisingly, although the case of linear polarization is extremely well documented in text books [16–18], the case of scattering circularly or elliptically polarized beams is not so well documented. More disturbingly, there are misleading and/or incorrect solutions to this problem given in fairly well-known references. In this paper a proper solution to the problem of the Compton scattering of circularly polarized light is presented in a reasonably

convenient general form. Our results are consistent with the recent discussion in Ref. [19].

The paper is organized as follows. In Section II, the spectral distribution of interest is defined and a single electron emission spectrum is derived for the full Compton effect. Next, in Section III, the method used to numerically integrate the individual electron spectra, and the method to add up and average the emission from a compressed bunch of electrons, are given. The main body of numerical results is presented in Sections IV and V. Here, a series of benchmarking studies and results are recorded, and a generalization of a scaling law discussed by several authors [1, 7, 12, 20] is given and verified numerically. In a previous publication [8], a calculation using the Thomson limit was documented. In Section VI this calculation is shown to be more appropriately completed using the full Compton recoil, and the modification of the emission spectrum in this case is documented. In Section VII the ODU compact Compton source design is evaluated by taking front-to-end simulation data of the beam produced at the interaction point in the source, and using it to predict the photon spectrum in collision. In the final technical section, Sec. VIII, the modifications needed to properly calculate the circularly polarized case are given. Finally, the importance of the new results is discussed and conclusions drawn in Section IX.

## II. ENERGY SPECTRAL DISTRIBUTIONS FOR THE FULL COMPTON EFFECT

Calculations of synchrotron radiation from various arrangements of magnets has an extensive literature. The result of Coisson on the energy spectral distribution of synchrotron radiation produced by an electron traversing a “short” magnet is a convenient starting point for our calculations [21]. In MKS units and translating his expressions into the symbols used in this paper, the result for the spectrum of the energy radiated by a single particle  $U_\gamma$  into a given solid angle  $d\Omega$  is (see [22] for more detailed discussion and cgs expressions)

$$\frac{d^2U_\gamma}{d\omega'd\Omega} = \frac{r_e^2\epsilon_0c}{2\pi} \left| \tilde{B}[\omega'(1-\beta\cos\theta)/\beta c] \right|^2 \frac{(1-\beta\cos\theta)^2\sin^2\phi + (\cos\theta-\beta)^2\cos^2\phi}{\gamma^2(1-\beta\cos\theta)^4}, \quad (1)$$

where  $\tilde{B}$  is the spatial Fourier transform of the transverse magnetic field bending the electron evaluated in the lab frame, and the notation indicates the transform is evaluated at the Doppler shifted wave number  $\omega'(1-\beta\cos\theta)/c\beta$ . Here  $\epsilon_0$  is the free-space permittivity,  $r_e = e^2/(4\pi\epsilon_0mc^2)$  is the classical electron radius ( $\approx 2.82 \times 10^{-15}$  m),  $c$  is the velocity of light,  $\beta = v_z/c$  the relativistic longitudinal velocity, and  $\gamma = 1/\sqrt{1-\beta^2}$  is the usual relativistic factor. Following standard treatments [16–18],  $\omega'$  denotes the scattered photon angular frequency as measured in the lab frame, and  $\theta$  and  $\phi$  are the standard polar angles of the scattered radiation in a coordinate system whose  $z$ -axis is aligned with the electron velocity.

A similar expression applies for linear Thomson scattering. The energy spectral density of the output pulse scattered by an electron may be computed analytically in the linear Thomson backscatter limit as

$$\frac{d^2U_\gamma}{d\omega'd\Omega} = \frac{r_e^2\epsilon_0}{2\pi c} \left| \tilde{E}[\omega'(1-\beta\cos\theta)/c(1+\beta)] \right|^2 \frac{(1-\beta\cos\theta)^2\sin^2\phi + (\cos\theta-\beta)^2\cos^2\phi}{\gamma^2(1-\beta\cos\theta)^4}. \quad (2)$$

As will be shown below, in the Thomson limit the electron recoil is neglected in the scattering event. This limit is valid for many X-ray source designs (ours included), but starts to break down in some of the higher electron energy sources being considered [8, 12]. Thus, in this section, the spectral distribution is calculated including the full Compton recoil for plane wave incident laser pulses. Implicit in the derivations is that linear scattering applies,  $a(z) \ll 1$ , where  $a = eA_x/mc$  is the normalized vector potential for the incident pulse. This assumption will be adopted throughout this paper.

In the calculations of the scattered energy a semiclassical model for the wave function of the incident laser is taken and a plane wave model for this field is adopted. The latter assumption is justified in our work because the collision point source size in our designs is much smaller than the collimation aperture for the X-rays produced: there is relatively little error introduced in replacing the actual scattering angle with the angle to the observation location in the far field limit. In the plane wave approximation the vector potential and electric field of the incident laser pulse are represented as wave packets

$$A_x(z, t) = \frac{1}{2\pi} \int_{-\infty}^{\infty} \tilde{A}_x(\omega) e^{i\omega(z/c+t)} d\omega, \quad (3)$$

$$E_x(z, t) = -\frac{1}{2\pi} \int_{-\infty}^{\infty} i\omega \tilde{A}_x(\omega) e^{i\omega(z/c+t)} d\omega, \quad (4)$$

with

$$\tilde{A}_x(\omega) = \int_{-\infty}^{\infty} A_x(z=0, t) e^{-i\omega t} dt. \quad (5)$$

The power per unit area in the wave packet is

$$c \left[ \frac{\epsilon_0}{2} E_x^2(z, t) + \frac{B_y^2(z, t)}{2\mu_0} \right] = \epsilon_0 c E_x^2(z, t). \quad (6)$$

Because of Parseval's theorem, the time-integrated intensity or energy per area in the pulse passing by an electron moving along the  $z$ -axis of the coordinate system is

$$\int_{-\infty}^{\infty} E_x^2(z=0, t) dt = \frac{1}{2\pi} \int_{-\infty}^{\infty} |\tilde{E}_x(\omega)|^2 d\omega, \quad (7)$$

where  $\tilde{E}_x(\omega)$  now denotes the Fourier time transform of the incident pulse. The incident energy per unit angular frequency per unit area is thus

$$\frac{\epsilon_0 c}{2\pi} |\tilde{E}_x(\omega)|^2 = \frac{\epsilon_0 c}{2\pi} |\omega \tilde{A}_x(\omega)|^2. \quad (8)$$

Within a “semi-classical” analysis the number of incident photons per unit angular frequency per area is consequently

$$\frac{\epsilon_0 c}{2\pi} \frac{|\tilde{E}_x(\omega)|^2}{\hbar |\omega|}. \quad (9)$$

The number of scattered photons generated into a given solid angle  $d\Omega$  is

$$\frac{dN_{scat}}{d\Omega} = \int_{-\infty}^{\infty} \frac{\epsilon_0 c}{2\pi} \frac{|\tilde{E}_x(\omega)|^2}{\hbar |\omega|} \frac{d\sigma}{d\Omega} d\omega, \quad (10)$$

and, because the scattered photon has energy  $\hbar\omega'$ , the total scattered energy is

$$\frac{dU_\gamma}{d\Omega} = \int_{-\infty}^{\infty} \frac{\epsilon_0 c}{2\pi} |\tilde{E}_x(\omega)|^2 \frac{\omega'}{\omega} \frac{d\sigma}{d\Omega} d\omega \quad (11)$$

where the Klein-Nishina differential cross section  $d\sigma/d\Omega$  will be used in the computations as discussed below. In any particular direction there is a unique monotonic relationship between  $\omega'$  and  $\omega$  and so a change of variables is possible yielding

$$\frac{d^2 U_\gamma}{d\omega' d\Omega} = \frac{\epsilon_0 c}{2\pi} |\tilde{E}_x(\omega(\omega'))|^2 \frac{d\sigma}{d\Omega} \left[ \frac{\omega'}{\omega} \frac{d\omega}{d\omega'} \right]. \quad (12)$$

Next the fact that the electron bunch has non-zero emittance and energy spread must be accounted for. The easiest way to accomplish this task is, for every electron in the bunch: (i) Lorentz transform the incident wave packet to the electron rest frame, (ii) Lorentz transform the propagation vector and polarization vector of the scattered wave into the electron frame, (iii) use the standard rest frame Klein-Nishina cross section to calculate the scattering from the electron in the lab frame, and (iv) sum the scattered energy of each individual electron. Therefore, one needs to evaluate and vary the scattering cross section slightly differently for each electron. The next task in this section is to give the general expression for the differential cross section for any possible kinematic condition for the electron.

For an electron at rest (beam rest frame), the Klein-Nishina differential scattering cross section for linearly polarized incident and scattered photons is

$$\frac{d\sigma}{d\Omega_b} = \frac{r_e^2}{4} \left( \frac{\omega'_b}{\omega_b} \right)^2 \left[ \frac{\omega'_b}{\omega_b} + \frac{\omega_b}{\omega'_b} - 2 + 4(\epsilon_b \cdot \epsilon'_b)^2 \right], \quad (13)$$

where  $\omega_b$  and  $\omega'_b$  are the incident and scattered radiation angular frequencies, respectively, with polarization 4-vectors  $\epsilon_b$  and  $\epsilon'_b$ . For future reference, the subscript  $b$  indicates a rest frame (beam frame) quantity, and throughout this

paper polarization 4-vectors are of the form  $\varepsilon = (0, \boldsymbol{\varepsilon})$ . We use the metric with signature  $(1, -1, -1, -1)$ , so that the invariant scalar product of two 4-vectors  $v_1^\mu$  and  $v_2^\mu$  is  $v_1 \cdot v_2 = v_1^0 v_2^0 - \mathbf{v}_1 \cdot \mathbf{v}_2$ . The results of the scattering from each electron in a beam will be summed incoherently.

For notational convenience, the (implicit) summation over the individual electron coordinates is suppressed in the foregoing expressions. In our final summations to obtain observables in the lab frame, the relativistic factors  $\boldsymbol{\beta}$  and  $\gamma$  will apply to specific electrons. Straightforward Lorentz transformation from the rest frame of the individual beam electrons to the lab frame are made. For example, the energy-momentum 4-vectors of the incident ( $k^\mu = (\omega, \mathbf{k})$ ) and scattered ( $k'^\mu = (\omega', \mathbf{k}')$ ) photons transform as

$$\begin{aligned}\omega_b &= \gamma(1 - \boldsymbol{\beta} \cdot \hat{\mathbf{k}})\omega, \\ \mathbf{k}_b &= -\gamma\boldsymbol{\beta}\omega + \omega\hat{\mathbf{k}} + \omega\frac{(\gamma-1)}{\beta^2}(\boldsymbol{\beta} \cdot \hat{\mathbf{k}})\boldsymbol{\beta}, \\ \omega'_b &= \gamma(1 - \boldsymbol{\beta} \cdot \hat{\mathbf{k}}')\omega', \\ \mathbf{k}'_b &= -\gamma\boldsymbol{\beta}\omega' + \omega'\hat{\mathbf{k}}' + \omega'\frac{(\gamma-1)}{\beta^2}(\boldsymbol{\beta} \cdot \hat{\mathbf{k}}')\boldsymbol{\beta},\end{aligned}\tag{14}$$

where  $\hat{\mathbf{k}} = \mathbf{k}/|\mathbf{k}|$ . Because the invariant scalar products  $k \cdot k$  and  $k' \cdot k'$  vanish, it readily follows that

$$\begin{aligned}\mathbf{k}_b \cdot \mathbf{k}_b &= \gamma^2(1 - \boldsymbol{\beta} \cdot \hat{\mathbf{k}})^2\omega^2 \rightarrow \hat{\mathbf{k}}_b = \frac{1}{\gamma(1 - \boldsymbol{\beta} \cdot \hat{\mathbf{k}})} \left( -\gamma\boldsymbol{\beta} + \hat{\mathbf{k}} + \frac{(\gamma-1)}{\beta^2}(\boldsymbol{\beta} \cdot \hat{\mathbf{k}})\boldsymbol{\beta} \right), \\ \mathbf{k}'_b \cdot \mathbf{k}'_b &= \gamma^2(1 - \boldsymbol{\beta} \cdot \hat{\mathbf{k}}')^2\omega'^2 \rightarrow \hat{\mathbf{k}}'_b = \frac{1}{\gamma(1 - \boldsymbol{\beta} \cdot \hat{\mathbf{k}}')} \left( -\gamma\boldsymbol{\beta} + \hat{\mathbf{k}}' + \frac{(\gamma-1)}{\beta^2}(\boldsymbol{\beta} \cdot \hat{\mathbf{k}}')\boldsymbol{\beta} \right),\end{aligned}\tag{15}$$

relating the unit propagation vectors in the electron rest frame to those in the lab frame.

The potential 4-vectors for the incident and scattered photons in the lab frame are  $(0, \boldsymbol{\varepsilon})Ae^{i(\omega t - \mathbf{k} \cdot \mathbf{x})}$  and  $(0, \boldsymbol{\varepsilon}')A'e^{i(\omega' t - \mathbf{k}' \cdot \mathbf{x})}$ . Using the 4-vector transformation formula and performing a gauge transformation to eliminate their zeroth components lead to  $(0, \boldsymbol{\varepsilon}_b)Ae^{i(\omega_b t_b - \mathbf{k}_b \cdot \mathbf{x}_b)}$  and  $(0, \boldsymbol{\varepsilon}'_b)A'e^{i(\omega'_b t_b - \mathbf{k}'_b \cdot \mathbf{x}_b)}$  where

$$\begin{aligned}\boldsymbol{\varepsilon}_b &= \gamma(\boldsymbol{\beta} \cdot \boldsymbol{\varepsilon})\hat{\mathbf{k}}_b + \boldsymbol{\varepsilon} + \frac{(\gamma-1)}{\beta^2}(\boldsymbol{\beta} \cdot \boldsymbol{\varepsilon})\boldsymbol{\beta}, \\ \boldsymbol{\varepsilon}'_b &= \gamma(\boldsymbol{\beta} \cdot \boldsymbol{\varepsilon}')\hat{\mathbf{k}}'_b + \boldsymbol{\varepsilon}' + \frac{(\gamma-1)}{\beta^2}(\boldsymbol{\beta} \cdot \boldsymbol{\varepsilon}')\boldsymbol{\beta}.\end{aligned}\tag{16}$$

Because the beam frame polarization vector is linearly related to the lab frame polarization vector, equivalent expressions apply to the transformation of the complex polarization vectors needed for describing circular or elliptical polarization which will be used in Section VIII. To evaluate the Klein-Nishina cross section, one can use the relation

$$\boldsymbol{\varepsilon}_b \cdot \boldsymbol{\varepsilon}'_b = \boldsymbol{\varepsilon} \cdot \boldsymbol{\varepsilon}' + \frac{(\boldsymbol{\beta} \cdot \boldsymbol{\varepsilon})(\hat{\mathbf{k}} \cdot \boldsymbol{\varepsilon}')}{(1 - \boldsymbol{\beta} \cdot \hat{\mathbf{k}})} + \frac{(\boldsymbol{\beta} \cdot \boldsymbol{\varepsilon}')(\hat{\mathbf{k}}' \cdot \boldsymbol{\varepsilon})}{(1 - \boldsymbol{\beta} \cdot \hat{\mathbf{k}}')} + \gamma^2(\boldsymbol{\beta} \cdot \boldsymbol{\varepsilon})(\boldsymbol{\beta} \cdot \boldsymbol{\varepsilon}')(\hat{\mathbf{k}}_b \cdot \hat{\mathbf{k}}'_b - 1).\tag{17}$$

Rewriting in terms of the 4-scalar product yields

$$\boldsymbol{\varepsilon}_b \cdot \boldsymbol{\varepsilon}'_b = \boldsymbol{\varepsilon} \cdot \boldsymbol{\varepsilon}' - \frac{(p_i \cdot \boldsymbol{\varepsilon})(k \cdot \boldsymbol{\varepsilon}')}{p_i \cdot k} - \frac{(p_i \cdot \boldsymbol{\varepsilon}')(k' \cdot \boldsymbol{\varepsilon})}{p_i \cdot k'} + \frac{(p_i \cdot \boldsymbol{\varepsilon})(p_i \cdot \boldsymbol{\varepsilon}')(k \cdot k')}{(p_i \cdot k)(p_i \cdot k')} \equiv P(\boldsymbol{\varepsilon}, \boldsymbol{\varepsilon}'),\tag{18}$$

where  $p_i$  is the 4-momentum of the incident electron. Note that because the 4-vectors  $p_i$ ,  $k$ , and  $k'$  are real, one has  $P(\boldsymbol{\varepsilon}_1, \boldsymbol{\varepsilon}_2^*) = P^*(\boldsymbol{\varepsilon}_1^*, \boldsymbol{\varepsilon}_2)$  and  $P(\boldsymbol{\varepsilon}_1^*, \boldsymbol{\varepsilon}_2^*) = P^*(\boldsymbol{\varepsilon}_1, \boldsymbol{\varepsilon}_2)$ .

The standard calculation of the lab frame phase-space factor yields the generalized Compton formula

$$\omega' = \frac{\omega(1 - \boldsymbol{\beta} \cdot \hat{\mathbf{k}})}{1 - \boldsymbol{\beta} \cdot \hat{\mathbf{k}}' + (\hbar\omega/\gamma mc^2)(1 - \hat{\mathbf{k}} \cdot \hat{\mathbf{k}}')}\tag{19}$$

and the expression for the lab frame cross section is

$$\frac{d\sigma}{d\Omega} = \frac{r_e^2}{4\gamma^2(1 - \boldsymbol{\beta} \cdot \hat{\mathbf{k}})^2} \left( \frac{\omega'}{\omega} \right)^2 \left[ \frac{\omega'(1 - \boldsymbol{\beta} \cdot \hat{\mathbf{k}}')}{\omega(1 - \boldsymbol{\beta} \cdot \hat{\mathbf{k}})} + \frac{\omega(1 - \boldsymbol{\beta} \cdot \hat{\mathbf{k}})}{\omega'(1 - \boldsymbol{\beta} \cdot \hat{\mathbf{k}}')} - 2 + 4[P(\boldsymbol{\varepsilon}, \boldsymbol{\varepsilon}')]^2 \right].\tag{20}$$

When  $\boldsymbol{\beta} = 0$  this expression obviously reduces to the rest frame result, and applies when a linearly polarized laser beam is scattered by an unpolarized electron beam. It captures the dependence on linear polarization in both the



initial and final states. The expression in Eq. (20) is a modification of a result found in Ref. [23]. Because the cross section is written here in terms of the incident electron and photon momenta, and in most Compton sources the recoil electron is not detected, this form is most convenient for integrating over the beam electron and incident laser photon distributions.

In our numerical calculations it is assumed that the polarization of the scattered photons is not observed. In this case the total cross section is the sum of the cross sections for scattering into the two orthonormal final state polarization vectors. The polarization sums may be replaced by scalar products as usual [24]. Defining

$$P^\mu(\varepsilon) \equiv \varepsilon^\mu - \frac{p_i \cdot \varepsilon}{p_i \cdot k} k^\mu - \frac{k' \cdot \varepsilon}{p_i \cdot k'} p_i^\mu + \frac{(p_i \cdot \varepsilon)(k \cdot k')}{(p_i \cdot k)(p_i \cdot k')} p_i^\mu, \quad (21)$$

one can write the scalar product in Eq. (18) as  $P(\varepsilon, \varepsilon') = P^\mu(\varepsilon)\varepsilon'_\mu$ . Because  $P^\mu(\varepsilon)k'_\mu = 0$ , one has

$$\begin{aligned} -P^\mu(\varepsilon)P_\mu(\varepsilon) &= P(\varepsilon, \varepsilon'_1)P(\varepsilon, \varepsilon'_1) + P(\varepsilon, \varepsilon'_2)P(\varepsilon, \varepsilon'_2) \\ &= 1 - m^2 c^2 \left[ \frac{(k' \cdot \varepsilon)(k' \cdot \varepsilon)}{(p_i \cdot k')^2} - 2 \frac{(p_i \cdot \varepsilon)(k' \cdot \varepsilon)}{(p_i \cdot k)(p_i \cdot k')^2} (k \cdot k') + \frac{(p_i \cdot \varepsilon)(p_i \cdot \varepsilon)}{(p_i \cdot k)^2 (p_i \cdot k')^2} (k \cdot k')^2 \right], \end{aligned} \quad (22)$$

for any two orthonormal polarization vectors  $\varepsilon'_1$  and  $\varepsilon'_2$  orthogonal to the propagation vector  $k'$ . The differential cross section summed over the final polarization is

$$\frac{d\sigma}{d\Omega} = \frac{r_e^2}{2\gamma^2(1 - \boldsymbol{\beta} \cdot \hat{\mathbf{k}})^2} \left( \frac{\omega'}{\omega} \right)^2 \left[ \frac{\omega'(1 - \boldsymbol{\beta} \cdot \hat{\mathbf{k}}')}{\omega(1 - \boldsymbol{\beta} \cdot \hat{\mathbf{k}})} + \frac{\omega(1 - \boldsymbol{\beta} \cdot \hat{\mathbf{k}})}{\omega'(1 - \boldsymbol{\beta} \cdot \hat{\mathbf{k}}')} - \frac{2m^2 c^2}{(p_i \cdot k')^2} \left( k' \cdot \varepsilon - \frac{(p_i \cdot \varepsilon)}{(p_i \cdot k)} k \cdot k' \right)^2 \right]. \quad (23)$$

This differential cross section, inserted in Eq. (12), is used to calculate the spectrum of the scattered radiation for a single electron. The total scattered energy is obtained by summing the spectra, each generated using the relativistic factors for each electron. A more general expression, correctly accounting for the circularly or elliptically polarized photons is presented in Section VIII. It should be noted that the individual and summed differential cross sections in Eqs. (20) and (23) are somewhat different from those reported in Ref. [12].

In order to determine the overall scale of the spectrum expected in the numerical results, and to provide contact with previous calculations, it is worthwhile to take the Thomson limit of these expressions. At low incident frequency, the recoil term involving the electron mass in Eq. (19) becomes negligible. The relationship between incident and scattered frequency is then

$$\omega' = \frac{\omega(1 - \boldsymbol{\beta} \cdot \hat{\mathbf{k}})}{1 - \boldsymbol{\beta} \cdot \hat{\mathbf{k}}'}, \quad (24)$$

and the expression for the lab frame cross section is

$$\frac{d\sigma}{d\Omega} = \frac{r_e^2}{\gamma^2(1 - \boldsymbol{\beta} \cdot \hat{\mathbf{k}}')^2} \left[ 1 - \frac{m^2 c^2}{(p_i \cdot k')^2} \left( k' \cdot \varepsilon - \frac{(p_i \cdot \varepsilon)}{(p_i \cdot k)} k \cdot k' \right)^2 \right]. \quad (25)$$

For an electron moving on the  $z$ -axis and backscattering with an  $x$ -polarized incident photon moving anti-parallel, the differential cross section simplifies to

$$\frac{d\sigma}{d\Omega} = \frac{r_e^2}{\gamma^2(1 - \beta \cos \theta)^2} \left[ \frac{(1 - \beta \cos \theta)^2 \sin^2 \phi + (\cos \theta - \beta)^2 \cos^2 \phi}{(1 - \beta \cos \theta)^2} \right], \quad (26)$$

consistent with Eq. (2) above.

Generally speaking, from an experimental point of view, it is most interesting to know the number of scattered photons per unit scattered energy. To determine this quantity note that, by the convolution theorem, the Fourier transform of the normalized vector potential function  $a_m(t) \cos(\omega_0 t)$  is

$$\tilde{a}(\omega) = \frac{\tilde{a}_m(\omega - \omega_0) + \tilde{a}_m(\omega + \omega_0)}{2}. \quad (27)$$

Therefore, after completing the trivial integrations over  $\phi$ ,

$$\frac{dU_\gamma}{d\omega'} = \frac{r_e^2 \varepsilon_0 c \pi}{8\pi} \left( \frac{mc}{e} \right)^2 \int \left( \frac{\omega'(1 - \beta \cos \theta)}{(1 + \beta)} \right)^2 \left| \tilde{a}_m \left( \frac{\omega'(1 - \beta \cos \theta)}{(1 + \beta)} \right) \right|^2 \left[ \frac{(1 - \beta \cos \theta)^2 + (\cos \theta - \beta)^2}{\gamma^2(1 - \beta \cos \theta)^4} \right] d(\cos \theta). \quad (28)$$

For an amplitude function slowly varying on the time scale of the oscillation, the Fourier transform of  $a_m$  is highly peaked as a function of  $\cos\theta$ . Changing variables, using Parseval's theorem to evaluate the frequency integral, and collecting constants yields [25]

$$\frac{dU_\gamma}{dE_\gamma} \doteq \frac{(1+\beta)c\alpha\pi}{4\beta\lambda} \frac{E_\gamma}{E_{\gamma,\max}} \left[ \frac{(1-\beta\cos\theta)^2 + (\cos\theta - \beta)^2}{(1-\beta\cos\theta)^2} \right] \int_{-\infty}^{\infty} a_m^2(t) dt, \quad (29)$$

where  $E_\gamma = \hbar\omega'$ ,  $E_{\gamma,\max} = (1+\beta)^2\gamma^2\hbar\omega_0$  is the Compton edge maximum energy emitted in the forward direction,  $\alpha$  is the fine structure constant, and  $\lambda = 2\pi c/\omega_0$  is the incident laser wavelength. The (equal) contributions from both positive and negative frequencies in the Fourier transform of the field are accounted in Eq. (29).

As a final step, replacing  $\cos\theta$  by  $E_\gamma$ , one obtains

$$\frac{dU_\gamma}{dE_\gamma} \doteq \frac{(1+\beta)c\alpha\pi}{4\beta^3\lambda} \frac{E_\gamma}{E_{\gamma,\max}} \left[ \beta^2 + \left( \frac{(1+\beta)E_\gamma}{E_{\gamma,\max}} - 1 \right)^2 \right] \int_{-\infty}^{\infty} a_m^2(t) dt. \quad (30)$$

The number density of all photons produced as a function of scattered energy is easily found from this equation simply by dividing by  $E_\gamma$ . The number distribution is precisely parabolic in the Thomson limit, with minimum value of  $\beta^2$  at  $E_\gamma = (1+\beta)\gamma^2\hbar\omega_{laser}$ , also the average energy of all photons. The number density grows to a value  $2\beta^2$  at both the Compton edge in the forward direction, and in the backward direction where the laser frequency is not Doppler shifted.

Equation (30) provides an excellent check of the scale for the results from the numerical technique. When the electron emittance and energy spread vanish, and one takes the long pulse limit, the height of the energy spectrum is

$$\frac{dU_\gamma}{dE_\gamma} \doteq \frac{c\alpha\pi}{\lambda} \int_{-\infty}^{\infty} a_m^2(t) dt, \quad (31)$$

and the height of the number spectrum is

$$\frac{dN_\gamma}{dE_\gamma} \doteq \frac{c\alpha\pi}{\lambda E_{\gamma,\max}} \int_{-\infty}^{\infty} a_m^2(t) dt, \quad (32)$$

at the Compton edge.

Throughout this work the plane wave approximation is used. However, at the expense of a greater number of computations for each electron, it is possible to capture three dimensional effects in the photon pulses using our general approach. The main adjustments are to modulate the vector potential because of the electron orbit through the three dimensional photon pulse structure and to include the arrival time variation of the individual electrons. A common incident photon spectrum for all of the electrons is no longer possible [26]. Our present intent is to undertake a more general code including such improvements and to publish calculations, including benchmarks, in a future publication. Presently, we anticipate that there may be computation time advantages from pursuing spectrum calculations using this approach compared to straight simulation calculations such as CAIN [27].

### III. NUMERICAL METHOD

In the previous section, we derived the general expression for energy density per solid angle for the Compton scattered photons from a laser beam by one electron, Eq. (12). The first non-constant term in Eq. (12) quantifies the electric field produced by the laser. The remaining terms are general and independent on the specifics of the experimental setup—the second non-constant term gives the probability that a photon is scattered into a given solid angle  $d\Omega$  and the third is the relativistic relationship between the frequencies of the incident and scattered radiation. Each of the non-constant terms depends on the scattered angular frequency  $\omega'$  and the solid angle  $d\Omega = d\phi d\cos\theta$ .

In order to compute the energy spectrum captured by a detector in a laboratory, the energy density per solid angle should be integrated over the solid angle of the aperture for a representative sample of particles from the electron beam. The resulting energy density spectrum for each electron is

$$\frac{dU_1}{d\omega'} = \frac{\epsilon_0 c}{2\pi} \int_0^{2\pi} d\phi \int_{\cos\theta_a}^1 \left| \tilde{E}(\omega(\omega')) \right|^2 \frac{d\sigma}{d\Omega} \left[ \frac{\omega'}{\omega} \frac{d\omega}{d\omega'} \right] d(\cos\theta), \quad (33)$$

where  $\theta_a$  is the semi-angle of the aperture and the subscript “1” denotes that the quantity is due to scattering off a single electron. Although essentially the same quantity is computed numerically by a somewhat different procedure

in Ref. [12], we have observed that integrating with  $\cos\theta$  as the independent variable markedly increases the precision of the numerical results. The equivalent number density of the spectrum is given by

$$\frac{dN_1}{d\omega'} = \frac{1}{\hbar\omega'} \frac{dU_1}{d\omega'}. \quad (34)$$

Only in the limiting case when the laser width approaches infinity and the pulse tends to a continuous wave (CW) is the integration over  $\cos\theta$  analytically tractable. In every other case, numerical integration of Eq. (33) is required.

For a representative subset of  $N_p$  particles from an electron beam distribution

$$f(\mathbf{p}) = \sum_{i=1}^{N_p} \delta(\mathbf{p} - \mathbf{p}_i), \quad (35)$$

where  $\mathbf{p} = (p_x, p_y, p_z)$ , the total energy density and number density spectra per electron are, respectively,

$$\frac{dU}{d\omega'} = \frac{1}{N_p} \sum_{i=1}^{N_p} \frac{dU_1}{d\omega'}(\mathbf{p}_i), \quad \frac{dN}{d\omega'} = \frac{1}{N_p} \sum_{i=1}^{N_p} \frac{dN_1}{d\omega'}(\mathbf{p}_i). \quad (36)$$

It is instructive to recall that the accuracy of results produced from a random sample on  $N_p$  particles is proportional to  $1/\sqrt{N_p}$ . Therefore, for example, for a 1% accuracy in computed spectra, an average over 10,000 points representing the underlying electron beam distribution is needed.

We implement the numerical integration of Eq. (36) in the `Python` scripting language [28]. The two-dimensional integration is performed using the `dblquad` routine from the `scipy` [29] scientific `Python` library. `dblquad` performs a two-dimensional integration by computing two nested one-dimensional quadratures using an adaptive, general-purpose integrator based on the `qag` routine from `QUADPACK` [30]. This general-purpose integrator performs well even for moderate-to-highly peaked electric fields  $\sigma \leq 200$ , where  $\sigma$  is the ratio of the length of the field falloff and the wavelength. For  $\lambda = 800$  nm this condition requires the laser pulse duration to be shorter than  $\tau = \sigma\lambda/c \approx 0.5$  ps. However, as the laser pulse duration increases beyond this approximate range, the electric field becomes extremely peaked, and the general purpose integrator `qag` can no longer handle this computation without occasionally generating spurious results. It simply is not designed to handle such extreme integrand behavior. Efforts are currently underway to replace the `qag` integrator with a state-of-the-art, intrinsically multidimensional, adaptive algorithm optimized to run on CPU and GPU platforms [31, 32].

Although the summation over electrons will be performed with an actual computer-generated distribution from the ODU Compton source design, it is worthwhile to summarize some facts about the numerical distributions for the electrons used in test cases to check the calculation method. The electron momenta are generated as

$$\begin{aligned} p_x &= p \sqrt{\frac{\varepsilon_x}{\beta_x^*}} \delta(0, 1), \\ p_y &= p \sqrt{\frac{\varepsilon_y}{\beta_y^*}} \delta(0, 1), \\ p_z &= \sqrt{[p + \sigma_p \delta(0, 1)]^2 - p_x^2 - p_y^2}, \end{aligned} \quad (37)$$

where  $p = \sqrt{p_x^2 + p_y^2 + p_z^2}$  is the magnitude of the total momentum,  $\delta(0, 1)$  is a Gaussian-distributed random variable with zero mean and unit variance and  $\sigma_p$  is the standard deviation in the total momentum:

$$\sigma_p = \sqrt{\left[E_0 \left(1 + \frac{\sigma_E}{E}\right)\right]^2 - m^2 c^4}. \quad (38)$$

Neglecting the small difference between the magnitude of the momentum and the  $z$ -component of the momentum,  $\sigma_{\theta_x} = \varepsilon_x/\beta_x^*$  and  $\sigma_{\theta_y} = \varepsilon_y/\beta_y^*$  are therefore the *rms* spread in beam transverse angles and  $\sigma_p$  is the relative longitudinal momentum spread. Using the relativistic energy-momentum relation in the ultrarelativistic limit and the usual statistical averaging, one obtains

$$\frac{\sigma_{E_e}}{E_e} = \sqrt{\sigma_p^2(1 - \sigma_{\theta_x}^2 - \sigma_{\theta_y}^2) + \sigma_{\theta_x}^4/2 + \sigma_{\theta_y}^4/2} \quad (39)$$

for the relative energy spread of the electrons generated including all terms up to fourth order in the small quantities  $\sigma_i$ . Notice that as the beam emittance changes there is a change in the energy spread generated at the same time.

TABLE I: Electron Beam and Incident Laser Pulse Parameters Used in Through-Aperture Spectra Calculation.

Parameter	Symbol	Value
Electron beam energy	$E_b$	500 MeV
Peak normalized vector potential	$a_0$	0.026
Incident photon spread parameter	$\sigma$	50
Peak laser pulse wavelength	$\lambda$	800 nm
Aperture distance from collision	$L$	60 m
Horizontal emittance	$\varepsilon_x$	0.05 nm rad
Vertical emittance	$\varepsilon_y$	0 nm rad
Electron energy spread	$\sigma_{E_e}/E_e$	$2 \times 10^{-3}$

The sheer amount of computation required to obtain the spectra with appropriate experimental (number of scattered energies  $E_\gamma$ ) and statistical (number of electrons sampling the distribution) resolution is substantial. This problem was alleviated by parallelizing the computation to efficiently run on multicore platforms. For this purpose, Python's `multiprocessing` library was used. The code is available upon request.

The code takes as input parameters of the inverse Compton scattering: (i) the properties of the electron beam (energy  $E_e$ , energy spread  $\sigma_E$ , horizontal emittance  $\varepsilon_x$ , vertical emittance  $\varepsilon_y$ , total charge  $Q$ ); (ii) the properties of the laser beam (energy  $E_l$ , energy spread  $\sigma$ , amplitude of the normalized vector potential  $a_0$ ); (iii) the shape of the laser beam (i.e., Gaussian, hard-edge, etc.); (iv) the properties of the aperture (size and location) and (v) the resolution of the simulation (the number of scattered radiation energies at which the spectrum is computed and the number of particles sampling the electron beam particle distribution). The output is the numerically computed scattered radiation spectrum.

#### IV. MODEL VALIDATION AND BENCHMARKING

The generalized Compton formula for the angular frequency  $\omega'$  in Eq. (19) can be written in more explicit form in the lab frame as

$$\omega'(\omega) = \frac{\omega(1 + \beta p_z/|\mathbf{p}|)}{1 - (\beta/|\mathbf{p}|)(p_x \sin \theta \cos \phi + p_y \sin \theta \sin \phi + p_z \cos \theta) + (\hbar\omega/\gamma mc^2)(1 + \cos \theta)}, \quad (40)$$

where  $\beta = |\boldsymbol{\beta}|$ . The greatest gain in angular frequency scattered is from an electron beam incident along  $\hat{z}$  and at  $\theta = 0$ , i.e., near the  $z$ -axis. We calculate the expected spectrum incident upon a circular, on-axis sensor aperture of radius  $R$  using Eq. (33). This geometry will be assumed in all the cases we consider.

It is evident that for a CW laser beam the Fourier transform of the electric field is simply a delta function. A pulsed laser model, in contrast, leads to a distribution in frequencies, with an intrinsic energy spread. The CW model, while useful in making the resulting spectra analytically tractable, does not allow for studying the effects of the pulsed nature of the laser beam. For instance, the relative importance of the energy spreads of the two colliding beams on the shape of the spectra of the backscattered radiation can only be addressed with a pulsed model. Here we consider a general pulsed structure of the incident laser beam.

The electric field can either be computed from the initially prescribed shape of the laser pulse or specified directly. In this paper and in the code, we provide one example of each: (i) electric field computed from the Gaussian laser pulse and (ii) electric field directly specified to be a hard-edge pulse, modeling a flat laser pulse.

Fourier transforming the Gaussian laser pulse

$$A_x(t) = A_0 \exp\left(-\frac{c^2 t^2}{2(\sigma\lambda)^2}\right) \cos\left(\frac{2\pi ct}{\lambda}\right), \quad (41)$$

yields the transformed electric field

$$\tilde{E}_x(\omega) = -i \frac{\omega A_0 \sigma \lambda}{c} \sqrt{\frac{\pi}{2}} \left[ \exp\left(-\frac{(\sigma\lambda)^2}{2c^2} \left(\omega - \frac{2\pi c}{\lambda}\right)^2\right) + \exp\left(-\frac{(\sigma\lambda)^2}{2c^2} \left(\omega + \frac{2\pi c}{\lambda}\right)^2\right) \right], \quad (42)$$

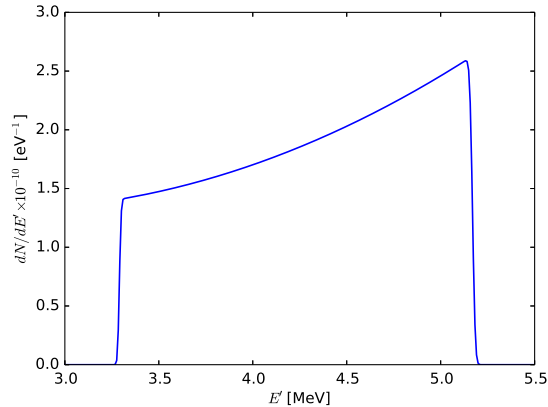


FIG. 1: The number density of the energy spectrum of a Compton gamma-ray beam produced by the head-on collision of a 466 MeV electron with a 789 nm laser beam, as in Fig. 2 in Ref. [7]. A collimation aperture with radius  $R$  of 50 mm is placed a distance  $L$  of 60 m downstream from the collision point ( $\theta_a = \tan^{-1}(R/L)$ ). Here a Gaussian laser pulse with  $\sigma = 50$  is used, while the laser in Ref. [7] is a CW.

where  $A_0$  is the maximum amplitude of the vector potential, and we denote the normalized vector potential by  $a_0 = eA_0/mc$ . In the limit of  $\sigma \rightarrow \infty$ , the laser transitions from the pulsed to CW nature, the electric field becomes two  $\delta$ -functions at  $\omega = \pm 2\pi c/\lambda$  and earlier results such as those in Fig. 2 of Ref. [7] are recovered. Figure 1 shows the number density of the energy spectrum for a pulsed very-wide wave with  $\sigma = 50$ . The perfect agreement of the overall scale in the two plots, computed two different ways, validates our numerical approach to this problem. In addition, the calculation captures the main effect expected from frequency spread in the incident laser: both sharp edges in the spectrum should be washed out so that the transition happens on a relative frequency scale equal to the relative frequency spread in the pulse.

A hard-edge laser pulse, modeling a flat laser pulse, is given by

$$A_x(t) = A_0 \cos(2\pi ct/\lambda) [\Theta(t + N\lambda/2c) - \Theta(t - N\lambda/2c)], \quad (43)$$

where  $\Theta(x)$  is the Heaviside step function, and  $N$  is the number of periods of the laser within the hard-edge pulse. The corresponding transformed electric field is

$$\tilde{E}_x(\omega) = -i\omega A_0 \left[ \frac{\sin((\omega - 2\pi c/\lambda)N\lambda/2c)}{\omega - 2\pi c/\lambda} + \frac{\sin((\omega + 2\pi c/\lambda)N\lambda/2c)}{\omega + 2\pi c/\lambda} \right]. \quad (44)$$

Again, in the limit of  $N \rightarrow \infty$ , the laser transitions from the pulsed to CW nature, the electric field reduces to two delta functions and the earlier results are recovered. An identical plot to our Fig. 1 and Fig. 2 of Ref. [7] is produced for  $N = 50$ .

We further check our pulsed laser model by investigating its behavior with  $\sigma = 50$  against other results reported in Ref. [7] in cases when detector aperture, emittance, and the electron beam energy spread are varied. The dependence of the computed spectrum on detector aperture is shown in Fig. 2. The left panel is in near-perfect agreement with Fig. 3(b) of Ref. [7]; including the laser pulsing accounts for any slight differences observed. The right panel shows the non-normalized spectrum. Figure 3 captures the dependence of the computed spectrum on electron beam emittance. Again, the left panel is in near-perfect agreement with Fig. 4(a) of Ref. [7] and the right panel shows the spectrum in physical units. The dependence of the computed spectrum on electron beam energy spread is illustrated in Fig. 4. The left panel is in agreement with Fig. 4(b) of Ref. [7] and the right panel shows the non-normalized spectrum. Because we have been able to reproduce earlier results produced in an entirely different way with our code, we are highly confident in our numerical method.

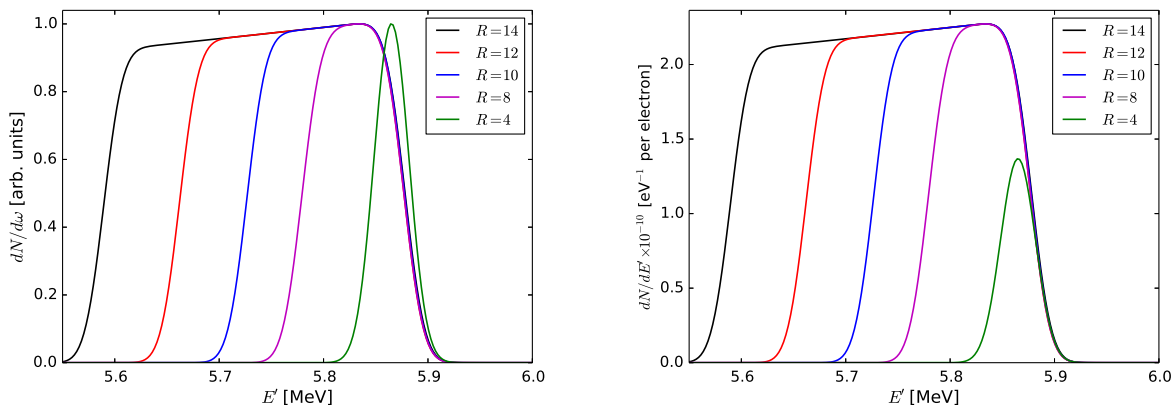


FIG. 2: The number density of the energy spectrum of a Compton gamma-ray beam produced by the head-on collision of a 500 MeV electron with a 800 nm pulsed laser beam, for different radii  $R$  of the collimation point (in mm), as in Fig. 3 in Ref. [7]. The aperture is 60 m downstream from the collision point. The horizontal emittance and energy spread of the electron beam are held constant at 0.05 nm rad and  $2 \times 10^{-3}$ , respectively. Here a Gaussian laser pulse with  $\sigma = 50$  is used, while the laser in Ref. [7] is a CW. Each curve is generated by averaging 400 electrons sampling the prescribed distribution. Left panel: Spectra scaled to their respective peak values (compare with Fig. 3(b) of Ref. [7]). Right panel: Spectra in physical units.

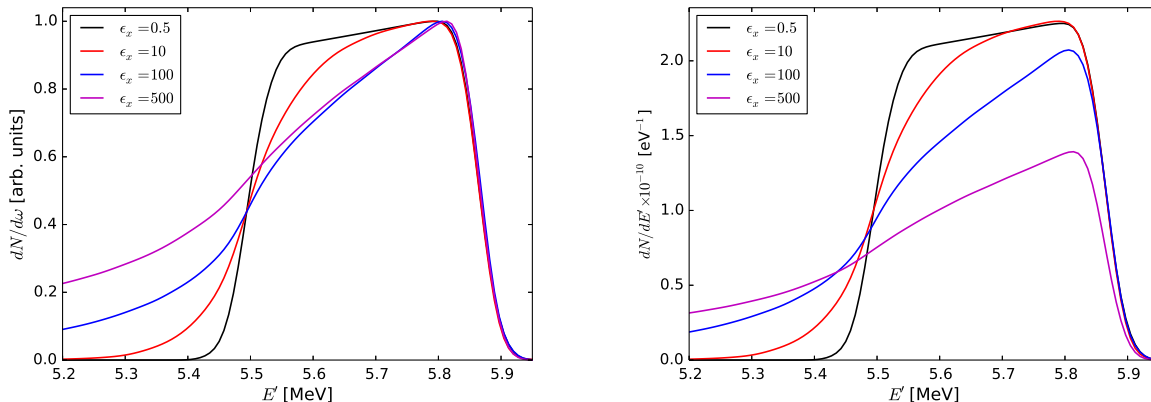


FIG. 3: The number density of the energy spectrum of a Compton gamma-ray beam produced by the head-on collision of a 500 MeV electron with a 800 nm pulsed laser beam, for different horizontal emittances  $\epsilon_x$  as in Fig. 4(a) in Ref. [7]. The laser is collimated by an aperture with radius of 16 mm, placed 60 m downstream from the collision point. The relative energy spread of the electron beam  $\sigma_E$  is held constant at  $2 \times 10^{-3}$ . Here a Gaussian laser pulse with  $\sigma = 50$  is used, while the laser in Ref. [7] is a CW. Each curve is generated by averaging 400 electrons sampling the prescribed distribution. Left panel: Spectra scaled to their respective peak values (compare with Fig. 4(a) of Ref. [7]). Right panel: Spectra in physical units.

## V. SCALING OF SCATTERED PHOTON ENERGY SPREAD

The effects of the energy spreads in the two colliding beam— $\sigma_{E_e}/E_e$  for the electron beam and  $\sigma_{E_p}/E_p$  for the incident photon beam—on the linewidth of the scattered radiation have been estimated from first principles [7] as

$$\frac{\sigma_{E'}}{E'} \approx \sqrt{\left(2\frac{\sigma_{E_e}}{E_e}\right)^2 + \left(\frac{\sigma_{E_p}}{E_p}\right)^2}, \quad (45)$$



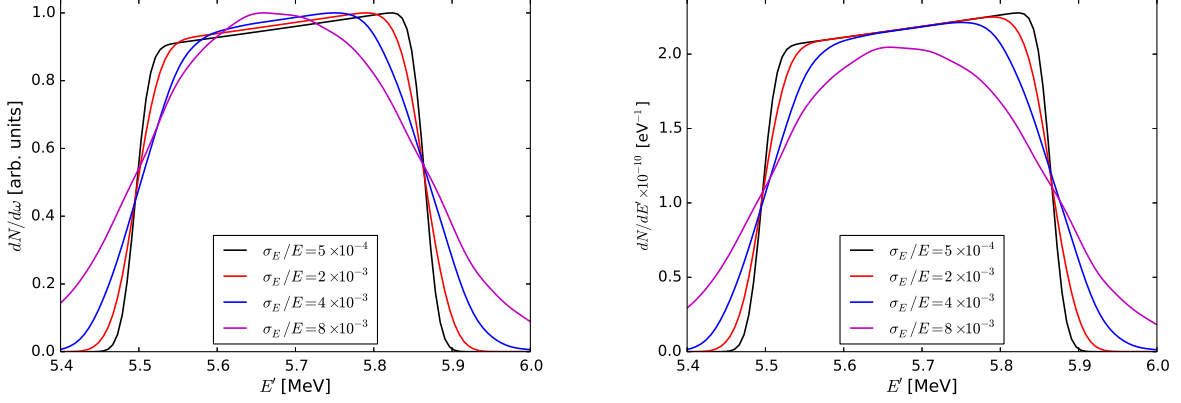


FIG. 4: The number density of the energy spectrum of a Compton gamma-ray beam produced by the head-on collision of a 500 MeV electron with a 800 nm pulsed laser beam, for different relative energy spread of the electron beam  $\sigma_E$  as in Fig. 4(b) in Ref. [7]. The laser is collimated by an aperture with radius of 16 mm, placed 60 m downstream from the collision point. The horizontal emittance  $\epsilon_E$  is held constant at 0.05 nm rad. Here a Gaussian laser pulse with  $\sigma = 50$  is used, while the laser in Ref. [7] is a CW. Each curve is generated by averaging 400 electrons sampling the prescribed distribution. Left panel: Spectra scaled to their respective peak values (compare with Fig. 4(b) of Ref. [7]). Right panel: Spectra in physical units.

where for our Gaussian model one can show

$$\frac{\sigma_{E_p}}{E_p} = \frac{1}{2\sqrt{2}\pi\sigma}, \quad (46)$$

However, this equation does not account for the intrinsic energy spread of the aperture  $\sigma_a/E_a$ . A more complete expression which takes this effect into consideration is

$$\frac{\sigma_{E'}}{E'} \approx \sqrt{\left(2\frac{\sigma_E}{E_e}\right)^2 + \left(\frac{\sigma_{E_p}}{E_p}\right)^2 + \left(\frac{\sigma_a}{E_a}\right)^2} \quad (47)$$

with the aperture energy spread

$$\frac{\sigma_a}{E_a} = \frac{\omega'_{\max} - \omega'_{\min}}{\sqrt{12} \omega'_{\text{mid}}}, \quad (48)$$

and

$$\begin{aligned} \omega'_{\max} &= \omega'(\theta = 0) = \frac{\omega(1 + \beta)}{1 - \beta + (2\hbar\omega/\gamma mc^2)}, \\ \omega'_{\min} &= \omega'(\theta = \theta_a) = \frac{\omega(1 + \beta)}{1 - \beta \cos(\theta_a) + (\hbar\omega/\gamma mc^2)(1 + \cos(\theta_a))}, \\ \omega'_{\text{mid}} &= \frac{(\omega'_{\max} + \omega'_{\min})}{2}. \end{aligned} \quad (49)$$

Equation (48) quantifies the relative *rms* energy spread of the approximately uniform distribution of frequencies passing the aperture when  $\sigma_{E_e}/E_e = 0$  and  $\sigma_{E_p}/E_p = 0$ . It follows directly from the fact that the *rms* width of a variable uniformly distributed between 0 and 1 is  $1/\sqrt{12}$ .

The energy spread due to emittance is [1]

$$\frac{\sigma_\epsilon}{E_e} = \frac{2\gamma^2\epsilon}{\beta^*}, \quad (50)$$

where  $\beta^*$  is the electron beta function at the interaction point. Because this contribution to the spread generates an asymmetrical low energy tail and a very non-Gaussian distribution, it does not as simply combine with the other sources.

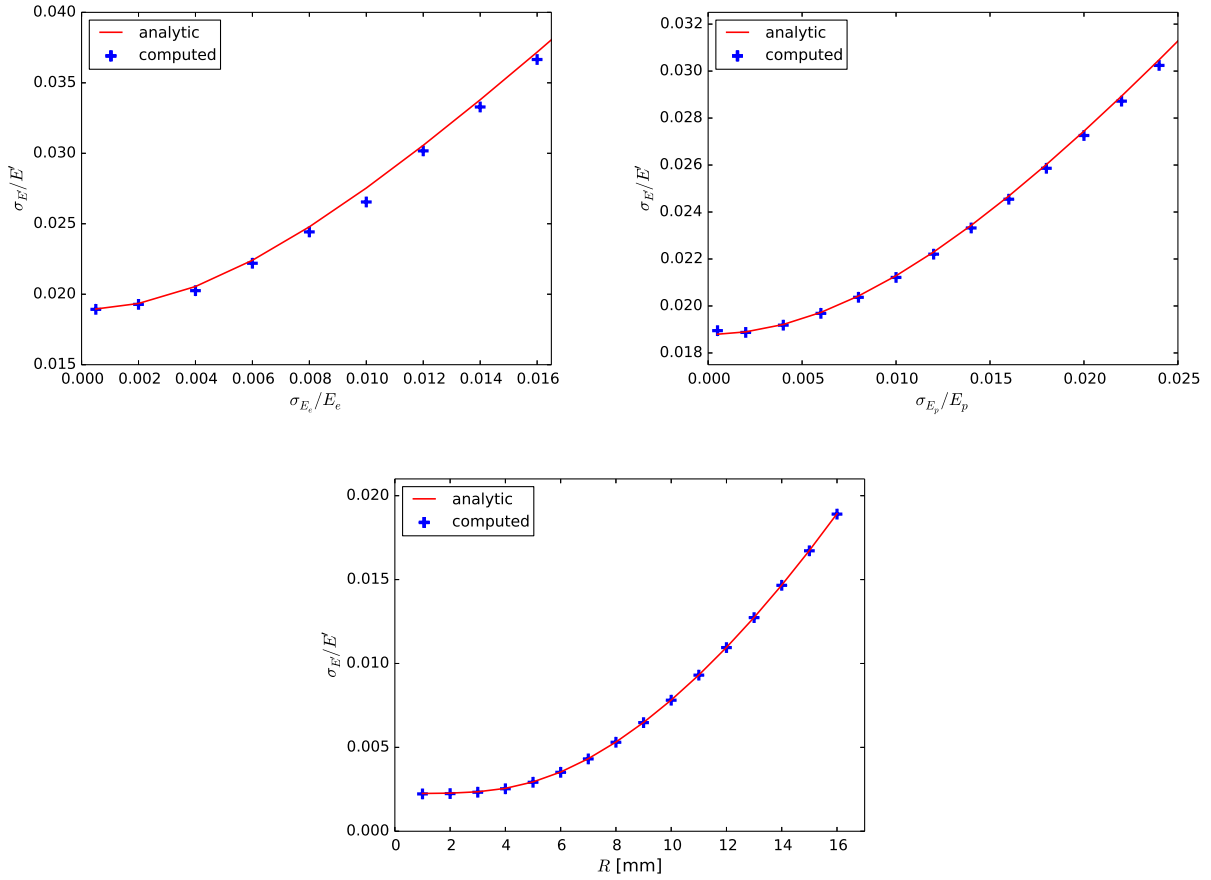


FIG. 5: Relationship between the energy spread of the two colliding beams— $\sigma_{E_e}/E_e$  for the electron beam and  $\sigma_{E_p}/E_p$  for the incident photon beam—and the energy spread of the scattered radiation  $\sigma_{E'}/E'$ : analytically predicted from Eq. (47) (red curves) and computed with our code (blue crosses). The parameters of the simulation are 500 MeV electron beam energy with a 800 nm pulsed laser beam, the horizontal emittance  $\epsilon_E = 0$ . The laser is collimated by an aperture with radius of 16 mm, placed 60 m downstream from the collision point. Each blue point is generated by averaging 1000 electrons sampling the prescribed distribution. Top left: Energy spread of the electron beam is varied; Gaussian laser pulse width is fixed at  $\sigma = 50$ , and aperture at 16 mm, placed 60 m downstream from the collision point. Top right: Energy spread of the laser beam is varied by changing its width in physical space; electron beam energy spread is held constant at  $\sigma_{E_e}/E_e = 0$  and aperture at 16 mm, placed 60 m downstream from the collision point. Bottom: Radius of the aperture  $R$  is varied; electron beam energy spread is held constant at  $\sigma_{E_e}/E_e = 0$ , photon beam at  $\sigma = 50$ .

Figure 5 shows a near-perfect agreement between the above estimate and the properties of the spectra computed with our pulsed formalism. The effect of varying the width of the laser pulse  $\sigma$  on the shape of the backscattered radiation spectrum is illustrated in Fig. 6. As the width of the laser pulse grows, the CW limit is entered, and the earlier results of Ref. [7] apply. For short pulses (small  $\sigma$ ), the energy spread of the laser pulse becomes so large that it dominates the backscattered spectral linewidth.

## VI. COMPTON FREQUENCY SHIFTING

The model presented in this paper properly includes the Compton recoil of the electrons. Including this effect is vital for working with high energy, relativistic photon-electron collisions. A series of calculations, based on parameters in two recent papers [8, 12], shows that Compton recoil is significant by comparing the full Compton calculation with that performed using the Thomson limit. The parameters are those from a recent paper by the Nebraska group [8], and from the new ELI - NP project in Bucharest [13].

Figure (7) clearly illustrates the Compton wavelength shifting. Both spectra are computed for the parameters

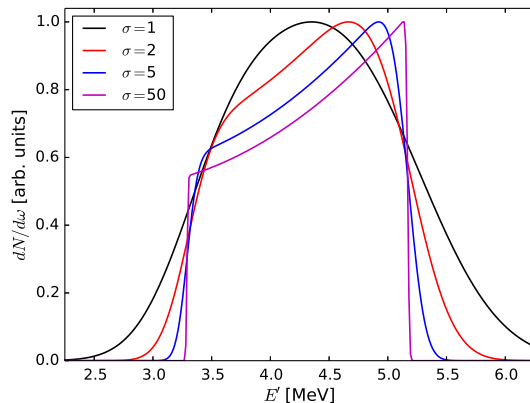


FIG. 6: Same as Fig. 1, only with varying width of the laser pulse  $\sigma$ .

TABLE II: Parameters used in the backscattering spectra. These parameters are very similar to the Ghebregziabher et al. [8] but the normalized vector potential has been reduced to bring the scattering event into the linear regime and eliminate the ponderomotive red shift and broadening.

Parameter	Symbol	Value
Aperture Semi-Angle		$1/(\gamma \times 10)$
Electron Beam Energy	$E_b$	300 MeV
Lorentz Factor	$\gamma$	587
Normalized Vector Potential	$a_0$	0.01
Peak Laser Pulse Wavelength	$\lambda$	800 nm
Standard Deviation of $a(t)$	$\sigma$	20.3

from Table II through very small apertures, the red plot using the correct Compton computation derived in this paper and the blue plot in the Thomson limit. For such photon-electron collisions, the electrons are well into the regime where relativistic effects are significant. Including Compton recoil decreases the scattered energy/frequency. At these electron and laser energies, the magnitude of the red shift is approximately 1% of the scattered photon energy. Although the focus of their paper is on other issues, care should be taken in quoting the X-ray line positions given in Ref. [8].

Frequency shifting from the recoiling electron must be properly included to predict the scattered radiation wavelength at ELI. The properties of ELI Beam A are listed in Table III. We used our new approach to compute spectra for the ELI project. Figure 8 shows spectra computed in both the Compton and Thomson regimes. For the higher energy electron beam, including recoil is clearly needed to properly account for the Compton wavelength and to obtain the correct energy in the scattered photons. Note that the Compton spectrum is different—most notably in its location in energy—from that reported in Ref. [12]. While the overall shape of the Compton spectrum is nicely reproduced in our calculation, there remains a difference in the scale which is due to an ambiguity in the definition of the aperture. Our calculations assume a full aperture  $\theta_a$  of 25  $\mu\text{rad}$ .

## VII. PROPOSED ODU COMPTON SOURCE

Superconducting RF linacs provide a means to a high average brilliance compact source of up to 12 keV X-rays. The ODU design is built on a pioneering vision developed in collaboration with scientists at MIT [33]. At present, the design has been developed to the point where full front-to-end simulations of the accelerator performance exist. The results of these simulations can be used to make predictions of the energy spectrum produced in an inverse Compton

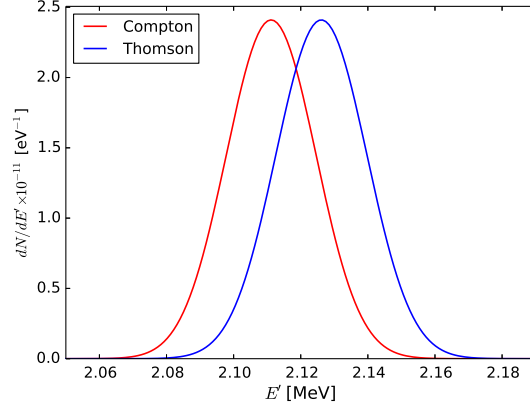


FIG. 7: Frequency shift between the spectra of Compton and Thomson scattering of a single electron with  $E_b = 300$  MeV, with a laser pulse with  $a_0 = 0.01$ ,  $\lambda = 800$  nm,  $s = 20.3$ , captured by aperture of  $A = 1/10\gamma$ .

TABLE III: Main parameters of electron and laser beams for ELI project [13].

Quantity	Unit	Beam A
Charge	C	$0.25 \times 10^{-9}$
Energy	MeV	360
Energy spread	MeV	0.234
Normalized horizontal emittance	mm mrad	0.65
Normalized vertical emittance	mm mrad	0.6
Laser wavelength	$\mu\text{m}$	0.523
Laser energy	J	1
Laser rms time duration	ps	4
Laser waist	$\mu\text{m}$	35

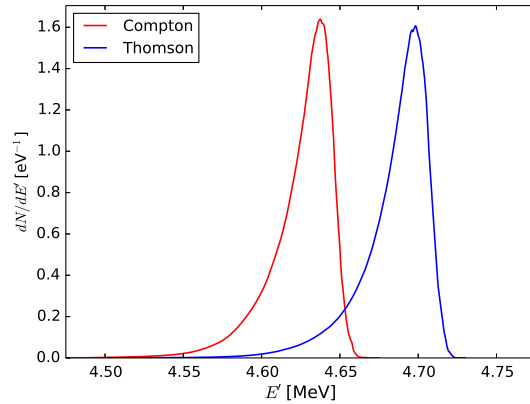


FIG. 8: Spectra—in both the Compton and Thomson regimes—for the ELI project, with parameters given in Table III. A total of 10,000 particles were used in generating this spectrum.

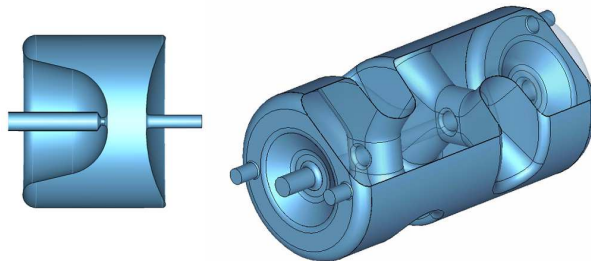


FIG. 9: A cross section picture of the SRF gun (left) and the SRF double-spoke accelerating cavity (right).

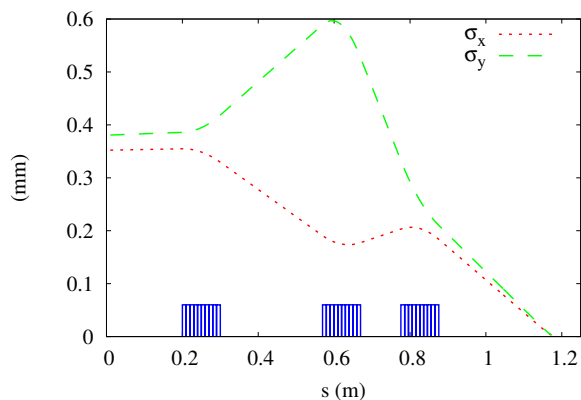


FIG. 10: The transverse spot size of the beam as it is focussed down into a small spot size.

source, and to help further optimize the source design by providing feedback on those elements of the design most important for achieving high brilliance.

### A. Design Elements

The ODU design consists of an accelerating section, operated at 500 MHz and 4.2 K, followed by a final focusing section comprised of three quadrupoles. The accelerating section begins with a re-entrant SRF gun, followed by four double-spoke SRF cavities. These two structures are shown in Fig. 9 [6].

The concept for the SRF gun was introduced over 20 years ago [34]. In the last ten years, the Naval Postgraduate School, Brookhaven National Lab, and University of Wisconsin have commissioned re-entrant SRF guns which operate at 4.2 K [35]. For the ODU design, it was needed to produce a bunch with ultra-low emittance, and the gun geometry was altered accordingly. The geometry was mainly altered around the nose-cone containing the cathode assembly, resulting in radial electric fields within the gun. These fields produce focusing of the bunch, making a solenoid for emittance compensation superfluous [6].

Until recently, accelerating electrons near the speed of light has not been attempted with multi-spoke cavities, largely because of the well-established and successful performance of TM-type cavities. However, multi-spoke cavities are familiar options for accelerating ions. Previous studies of multi-spoke cavities suggest strongly that they are a viable option for accelerating electrons [5, 36], and they provide a path to operating at 4.2 K through a low-frequency accelerator that is reasonably compact. The double-spoke cavities comprising the linear accelerator (linac) were designed by Christopher Hopper in an ODU dissertation [37, 38] and developed and tested in collaboration with Jefferson Lab [39, 40]. The bunch exiting the linac passes through three quadrupoles. Figure 10 shows the horizontal and vertical size of the bunch as it traverses the quadrupoles, before it is focused down to a small spot size. Table IV lists the properties of the bunch at the collision point.

TABLE IV: Properties of electron bunch at the collision point.

Parameter	Quantity	Units
kinetic energy	25.0	MeV
bunch charge	10.0	pC
<i>rms</i> energy spread	3.44	keV
$\epsilon_{x,\text{rms}}^N$	0.10	mm-mrad
$\epsilon_{y,\text{rms}}^N$	0.13	mm-mrad
$\sigma_x$	3.4	$\mu\text{m}$
$\sigma_y$	3.8	$\mu\text{m}$
$\beta_x$	5.4	mm
$\beta_y$	5.4	mm
FWHM bunch length	3	psec
$\sigma_z$	0.58	mm

### B. Tracking to Collision

The electromagnetic field modes of the SRF gun and the SRF double-spoke cavity are calculated by Superfish and CST MICROWAVE STUDIO (CST MWS) respectively [41, 42]. Utilizing these calculated electromagnetic fields, IMPACT-T tracked a defined particle bunch off the cathode and through the accelerating linac [43]. Afterwards, tools were used to translate the coordinates of the electrons in the bunch into the SDDS format `elegant` [44] requires, and `elegant` tracks the bunch as it traverses the three quadrupoles that comprise the final focusing section. Figure 11 shows simulation calculations of the beam spot and the longitudinal, horizontal, and vertical phase spaces at the collision point.

### C. X-ray Yield

The simulations were used to generate the beam distribution at collision as represented by 48,756 simulation particles. This distribution was then used to determine the scattered photon spectrum through various apertures. The resulting spectra are shown in Fig. 12, generated by colliding 4,000 particles from the ensemble of 48,756 tracked. The right panel of the figure shows the same spectra on the log scale, demonstrating that the accuracy of this calculation method allows one to evaluate the importance of the tails of the electron distribution on the final result. In addition, the radiation spectrum was calculated once with the full complement of electrons at the aperture of  $1/10\gamma$ , yielding negligible difference with the 4,000 particle calculation shown. With assumptions about the scattering laser, it is possible to determine the X-ray source that a head-on collision of these two beams will provide. We assumed a 1 MW circulating power laser, with a spot size of  $3.2 \mu\text{m}$  and a wavelength of  $1 \mu\text{m}$  [5].

Consistent with the very small transverse source size, the average brilliance of the photon beam is obtained from a pin-hole measurement

$$B = \lim_{\theta_a \rightarrow 0} \frac{F}{2\pi\sigma_x\sigma_y\pi\theta_a^2}, \quad (51)$$

where  $F$  is the number of photons in a 0.1% bandwidth transmitted through the aperture. Collecting the results from the  $1/40\gamma$  figure and remembering 0.1% of 12 keV is 12 eV, the maximum number of photons in a 0.1% bandwidth through the aperture is 600 at 10 pC. The average flux and brilliance for  $6.242 \times 10^{15}$  electrons per second (10 pC at 100 MHz) is shown in Table V. Essentially because of the small spot size in collision and the high repetition rate of collisions, this result is world-leading for Compton sources [45].

## VIII. ON THE CIRCULAR AND ELLIPTICALLY POLARIZED CASES

In the course of this work a question arose about the correct generalization of the Klein-Nishina formula for scattering of circularly polarized photons. After reviewing relevant literature, some of which was contradictory or incorrect, a



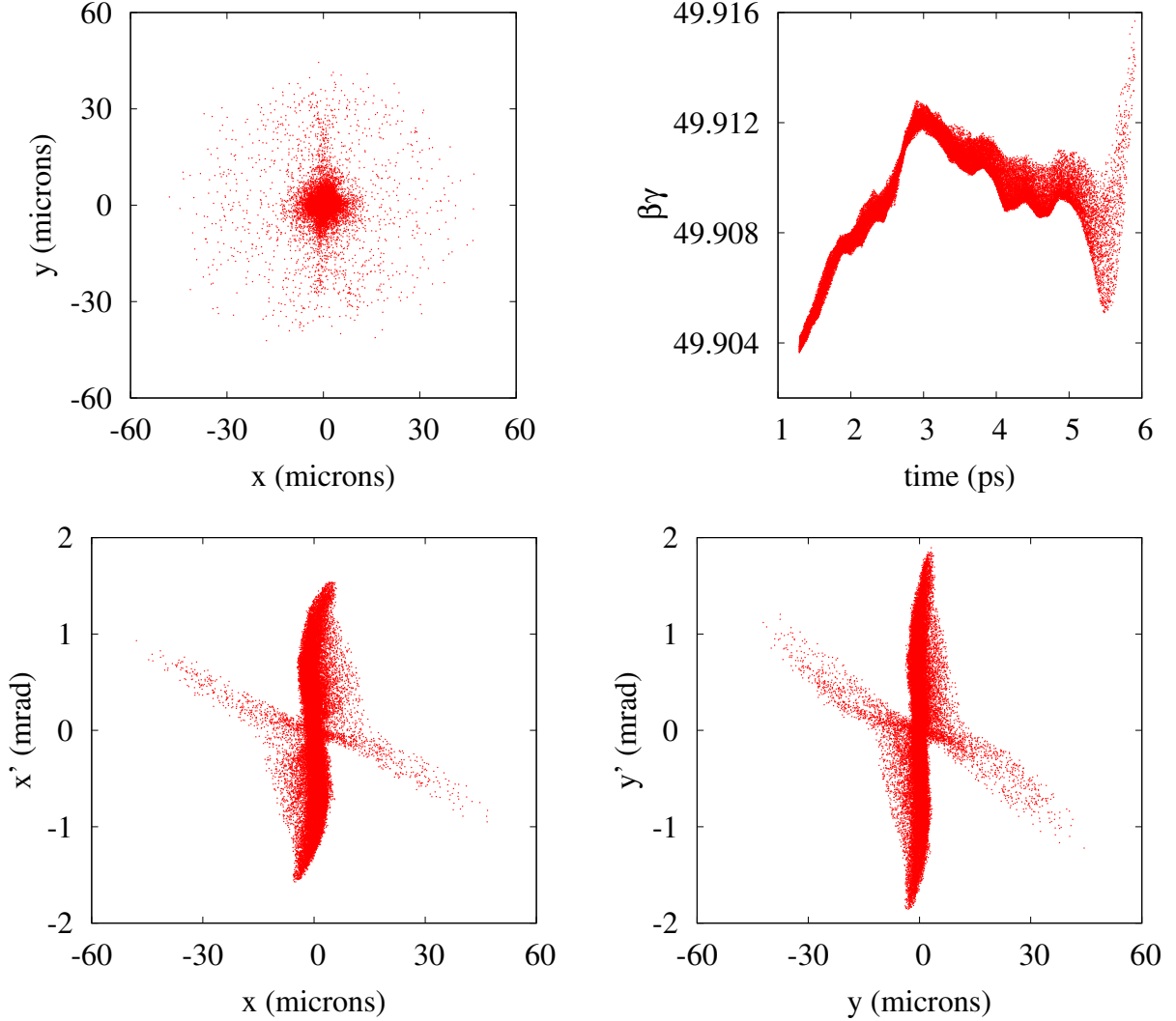


FIG. 11: The beam spot (upper left), longitudinal phase space (upper right), horizontal phase space (lower left), and vertical phase space (lower right) of the electron bunch at the collision point.

TABLE V: X-ray source properties.

Parameter	Quantity	Units
$N_\gamma$	$1.4 \times 10^6$	photons
Flux	$1.4 \times 10^{14}$	ph/sec
Full Flux in 0.1%BW	$2.1 \times 10^{11}$	ph/(s-0.1%BW)
Average brilliance	$1.0 \times 10^{15}$	ph/(s-mm <sup>2</sup> -mrad <sup>2</sup> -0.1%BW)

proper calculation was completed which is documented in this section. In particular, the calculation reduces to the correct beam-frame results given by Stedman and Pooke [46], but covers general kinematics as in the linearly polarized case above. Our concern is with scattering of polarized photons from unpolarized electrons. Others, concerned with electron polarimetry, have written out solutions for scattering from polarized electrons.

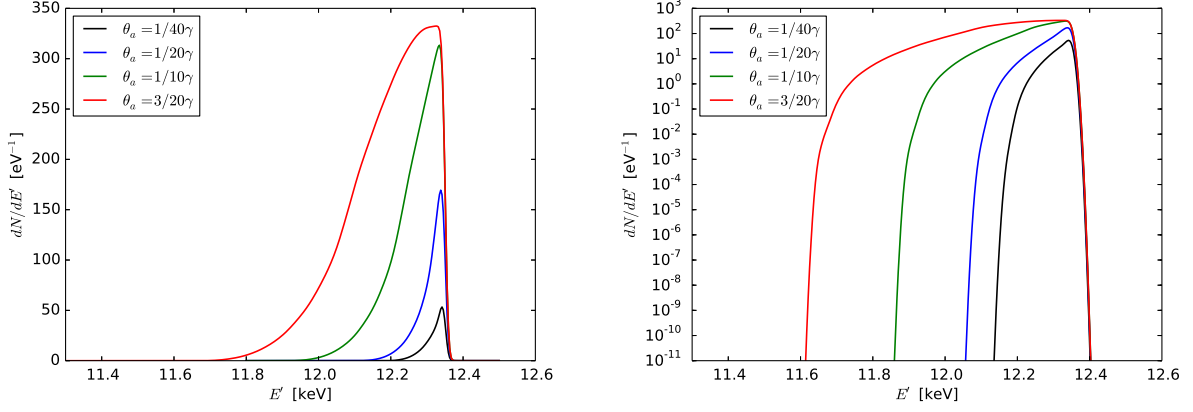


FIG. 12: Number spectra for the Old Dominion University Compton source with 10 pC electron bunch charge. Left: For apertures  $1/40\gamma$ ,  $1/20\gamma$ , and  $3/20\gamma$ , 4,000 particles were used in generating each curve. For aperture  $1/10\gamma$ , 48,756 particles were used in generating the plot. Right: The same as the panel on the left, except on the log scale.

The beam frame Klein-Nishina scattering differential cross section is sometimes presented as [47–49] [cf. Eq. (13)],

$$\frac{d\sigma}{d\Omega_b} = \frac{r_e^2}{4} \left( \frac{\omega'_b}{\omega_b} \right)^2 \left[ \frac{\omega'_b}{\omega_b} + \frac{\omega_b}{\omega'_b} - 2 + 4|\varepsilon_b \cdot \varepsilon_b'^*|^2 \right], \quad (52)$$

The fact that circular polarization is discussed elsewhere within all of these references might lead one to conclude that the formula is valid for general complex polarization vectors, e.g., for scattering of elliptically or circularly polarized lasers. This conclusion is incorrect; Eq. (52) has validity for linear polarization only because then the scalar product involves purely real polarization vectors and  $|\varepsilon_b \cdot \varepsilon_b'^*|^2 = (\varepsilon_b \cdot \varepsilon_b')^2$ , as above. However, the differential cross section in Eq. (52) is not valid for more general complex cases.

The proper beam frame differential cross section has been provided by Stedman and Pooke [46]

$$\frac{d\sigma}{d\Omega_b} = \frac{r_e^2}{4} \left( \frac{\omega'_b}{\omega_b} \right)^2 \left[ \left( \frac{\omega'_b}{\omega_b} + \frac{\omega_b}{\omega'_b} \right) \left( 1 - |\varepsilon_b \cdot \varepsilon_b'|^2 + |\varepsilon_b \cdot \varepsilon_b'^*|^2 \right) + 2 \left( |\varepsilon_b \cdot \varepsilon_b'|^2 + |\varepsilon_b \cdot \varepsilon_b'^*|^2 - 1 \right) \right]. \quad (53)$$

In addition, these authors point to the incorrect assumption leading to the derivation of Eq. (52) when complex polarization vectors are involved:  $(\varepsilon_{b\mu}\gamma^\mu)(\varepsilon_{b\nu}^*\gamma^\nu) \neq -1$  where the multiplication here is between the summed Dirac matrices. It has been verified that when the correct anti-commutator relation  $[\varepsilon_{b\mu}\gamma^\mu, \varepsilon_{b\nu}^*\gamma^\nu]_+ = 2\varepsilon_b \cdot \varepsilon_b^*$  is used when performing the traces to evaluate the differential cross section, Eq. (53) results. Clearly, for linear polarization  $\varepsilon_b = \varepsilon_b^*$  and  $\varepsilon_b' = \varepsilon_b'^*$ , and Eq. (53) leads directly to Eq. (13). Also, Eq. (53) is equivalent to the corrected expression

$$\frac{d\sigma}{d\Omega_b} = r_e^2 \left( \frac{\omega'_b}{\omega_b} \right)^2 \left[ |\varepsilon_b \cdot \varepsilon_b'^*|^2 + \frac{(\omega_b - \omega'_b)^2}{4\omega_b\omega_b'} \left( 1 + (\varepsilon_b \times \varepsilon_b^*) \cdot (\varepsilon_b' \times \varepsilon_b'^*) \right) \right], \quad (54)$$

which appears in the third edition of Jackson's text [50].

Clearly, the procedure followed in the linear polarization case translates here. The lab frame cross section may be written down by inspection

$$\frac{d\sigma}{d\Omega} = \frac{r_e^2}{4\gamma^2(1 - \boldsymbol{\beta} \cdot \hat{\mathbf{k}})^2} \left( \frac{\omega'}{\omega} \right)^2 \left[ \left( \frac{\omega'(1 - \boldsymbol{\beta} \cdot \hat{\mathbf{k}}')}{\omega(1 - \boldsymbol{\beta} \cdot \hat{\mathbf{k}})} + \frac{\omega(1 - \boldsymbol{\beta} \cdot \hat{\mathbf{k}})}{\omega'(1 - \boldsymbol{\beta} \cdot \hat{\mathbf{k}}')} \right) \left( 1 - |P(\varepsilon, \varepsilon')|^2 + |P(\varepsilon, \varepsilon'^*)|^2 \right) + 2 \left( |P(\varepsilon, \varepsilon')|^2 + |P(\varepsilon, \varepsilon'^*)|^2 - 1 \right) \right]. \quad (55)$$

This equation extends Eq. (20) to include cases with arbitrary complex polarization and agrees with Eq. (3) of Ref. [19] by applying energy-momentum conservation to eliminate  $p_f$ . In sources where a circularly polarized laser beam is scattered, but the final polarization is not observed, the polarization sum is modified. For general complex polarization

vectors Eq. (22) becomes

$$\begin{aligned}
-P^\mu(\varepsilon)P_\mu(\varepsilon^*) &= -P^\mu(\varepsilon)P_\mu^*(\varepsilon) = P(\varepsilon, \varepsilon'_1)P(\varepsilon^*, \varepsilon'^*_1) + P(\varepsilon, \varepsilon'_2)P(\varepsilon^*, \varepsilon'^*_2) \\
&= 1 - m^2c^2 \left[ \frac{(k' \cdot \varepsilon)(k' \cdot \varepsilon^*)}{(p_i \cdot k')^2} - \frac{(p_i \cdot \varepsilon)(k' \cdot \varepsilon^*) + (k' \cdot \varepsilon)(p_i \cdot \varepsilon^*)}{(p_i \cdot k)(p_i \cdot k')^2} (k \cdot k') + \frac{(p_i \cdot \varepsilon)(p_i \cdot \varepsilon^*)}{(p_i \cdot k)^2(p_i \cdot k')^2} (k \cdot k')^2 \right] \quad (56)
\end{aligned}$$

now for any two orthonormal complex polarization vectors  $\varepsilon'_1$  and  $\varepsilon'_2$  orthogonal to the propagation vector  $k'$ . Because Eq. (56) is identical under the interchange  $\varepsilon \leftrightarrow \varepsilon^*$ ,  $P(\varepsilon, \varepsilon'^*_1)P(\varepsilon^*, \varepsilon'_1) + P(\varepsilon, \varepsilon'^*_2)P(\varepsilon^*, \varepsilon'_2)$  evaluates identically, and the summed differential cross section is

$$\begin{aligned}
\frac{d\sigma}{d\Omega} &= \frac{r_e^2}{2\gamma^2(1 - \beta \cdot \hat{\mathbf{k}})^2} \left( \frac{\omega'}{\omega} \right)^2 \left[ \frac{\omega'(1 - \beta \cdot \hat{\mathbf{k}}')}{\omega(1 - \beta \cdot \hat{\mathbf{k}})} + \frac{\omega(1 - \beta \cdot \hat{\mathbf{k}})}{\omega'(1 - \beta \cdot \hat{\mathbf{k}}')} \right. \\
&\quad \left. - 2m^2c^2 \left( \frac{(k' \cdot \varepsilon)(k' \cdot \varepsilon^*)}{(p_i \cdot k')^2} - \frac{(p_i \cdot \varepsilon)(k' \cdot \varepsilon^*) + (k' \cdot \varepsilon)(p_i \cdot \varepsilon^*)}{(p_i \cdot k)(p_i \cdot k')^2} (k \cdot k') + \frac{(p_i \cdot \varepsilon)(p_i \cdot \varepsilon^*)}{(p_i \cdot k)^2(p_i \cdot k')^2} (k \cdot k')^2 \right) \right]. \quad (57)
\end{aligned}$$

It should be emphasized that this result is correct for circular polarization vectors and reduces to Eq. (23) for linear polarization. Equation (57) may be averaged over the initial spin by effecting initial polarization summations. The correct electron and photon spin-averaged differential cross section emerges [24, 51].

## IX. SUMMARY

In this paper a novel calculation prescription is used to determine the emission characteristics of the scattered radiation in a Compton back-scatter source. The model we have developed has been exercised to precisely calculate the photon energy distributions from Compton scattering events. The calculations are quite general, incorporating beam emittance, beam energy spread, laser photon spread, and the full Compton effect. The final form of the scattering distribution is quite convenient for computer implementation and simulation with computer-calculated electron beam distributions.

The calculations sum the full electron rest frame Klein-Nishina scattering cross section, suitably transformed to the lab frame, on an electron by electron basis. Although somewhat “brute-force” and moderately computationally expensive, such a calculational approach has several advantages. Firstly, the model accurately accounts for the details in the spectra that are generated from, e.g., non-Gaussian particle distributions or other complicated particle phase spaces. Secondly, it is straightforward to incorporate into the model pulsed incident lasers in the plane-wave approximation. And thirdly, and most significantly, the model is simple and straightforward to implement computationally. Any numerical problems we have observed in executing our computations have been due to causes easily understood and straightforwardly addressed.

As test and benchmarking cases, we have confirmed the results of the Duke group [7] and reconsidered a calculation of the Nebraska group [8], and corrected and confirmed a calculation made for ELI. In addition, we have numerically confirmed scaling laws for the photon energy spread emerging from Compton scattering events, and extended them to include apertures. When applied to numerical Gaussian pulsed photon beams and electron beams with Gaussian spreads, a scaling law for the scattered photon energy spread was verified through a series of numerical computations. This scaling law has been speculated on previously and has been shown to be valid over a wide range of physically interesting parameters.

A principal motivation for developing this approach is that we could analyze the performance of ODU’s compact SRF Compton X-ray source. Front-to-end design simulations have been completed that have been used to make detailed predictions of the photon flux and brilliance expected from the source. Based on the results we have found, SRF-based sources have the potential to produce substantial average brilliance, better than other types of Compton sources, and shown that the brilliance is mainly limited by the beam emittance.

Finally, we have recorded the proper cross sections to apply when the incident or scattered radiation are circularly polarized.

## Acknowledgments

This paper is authored by Jefferson Science Associates, LLC under U.S. Department of Energy (DOE) Contract No. DE-AC05-06OR23177. Additional support was provided by Department of Energy Office of Nuclear Physics Award No. DE-SC004094 and Basic Energy Sciences Award No. JLAB-BES11-01. E. J. and B. T. acknowledge the support of Old Dominion University Office of Research, Program for Undergraduate Research and Scholarship.

K. D. and J. R. D. were supported at ODU by Department of Energy Contract No. de-sc00004094. R. K. was supported by the NSF Research Experience for Undergraduates (REU) at Old Dominion University (Award No. 1359026). T. H. acknowledges the support from the U.S. Department of Energy, Science Undergraduate Laboratory Internship (SULI) program. This research used resources of the National Energy Research Scientific Center, which is supported by the Office of Science of the U.S. Department of Energy under Contract No. DE-AC02-05CH11231 The U.S. Government retains a non-exclusive, paid-up, irrevocable, world-wide license to publish or reproduce this manuscript for U.S. Government purposes.

- 
- [1] G. A. Krafft and G. Priebe, *Reviews of Accelerator Science and Technology* **03**, 147 (2010), URL <http://www.worldscientific.com/doi/abs/10.1142/S1793626810000440>.
- [2] Z. Huang and R. D. Ruth, *Phys. Rev. Lett.* **80**, 976 (1998), URL <http://link.aps.org/doi/10.1103/PhysRevLett.80.976>.
- [3] R. Pantell, G. Soncini, and H. Puthoff, *IEEE Journal of Quantum Electronics* **4**, 905 (1968), ISSN 0018-9197.
- [4] F. B. Bunkin, A. E. Kazakov, and M. V. Fedorov, *Soviet Physics Uspekhi* **15**, 416 (1973), URL <http://stacks.iop.org/0038-5670/15/i=4/a=R04>.
- [5] K. Deitrick, J. R. Delayen, B. R. P. Gamage, K. Henrandez, C. Hopper, G. A. Krafft, R. Olave, and T. Satogata (2013), URL <http://toddsatogata.net/Papers/2013-09-03-ComptonSource-2up.pdf>.
- [6] K. Deitrick, J. R. Delayen, B. R. P. Gamage, G. A. Krafft, and T. Satogata, *Proceedings of IPAC2015* p. 1706 (2015), URL <http://accelconf.web.cern.ch/AccelConf/IPAC2015/papers/tupje041.pdf>.
- [7] C. Sun, J. Li, G. Rusev, A. P. Tonchev, and Y. K. Wu, *Phys. Rev. ST Accel. Beams* **12**, 062801 (2009), URL <http://link.aps.org/doi/10.1103/PhysRevSTAB.12.062801>.
- [8] I. Ghebregziabher, B. A. Shadwick, and D. Umstadter, *Phys. Rev. ST Accel. Beams* **16**, 030705 (2013), URL <http://link.aps.org/doi/10.1103/PhysRevSTAB.16.030705>.
- [9] W. J. Brown and F. V. Hartemann, *Phys. Rev. ST Accel. Beams* **7**, 060703 (2004), URL <http://link.aps.org/doi/10.1103/PhysRevSTAB.7.060703>.
- [10] F. V. Hartemann and S. S. Q. Wu, *Phys. Rev. Lett.* **111**, 044801 (2013), URL <http://link.aps.org/doi/10.1103/PhysRevLett.111.044801>.
- [11] E. Esarey, S. K. Ride, and P. Sprangle, *Phys. Rev. E* **48**, 3003 (1993), URL <http://link.aps.org/doi/10.1103/PhysRevE.48.3003>.
- [12] V. Petrillo, A. Bacci, R. B. A. Zinati, I. Chaikovska, C. Curatolo, M. Ferrario, C. Maroli, C. Ronsivalle, A. Rossi, L. Serafini, et al., *Nuclear Instruments and Methods in Physics Research Section A: Accelerators, Spectrometers, Detectors and Associated Equipment* **693**, 109 (2012), ISSN 0168-9002, URL <http://www.sciencedirect.com/science/article/pii/S0168900212007772>.
- [13] C. Vaccarezza et al, *Proceedings of IPAC2012* pp. 1086–1088 (2012), URL <http://accelconf.web.cern.ch/AccelConf/IPAC2012/paper>
- [14] O. Klein and Y. Nishina, *Zeitschrift für Physik* **52**, 853 (1929), ISSN 0044-3328, URL <http://dx.doi.org/10.1007/BF01366453>.
- [15] B. Terzić, K. Deitrick, A. S. Hoffer, and G. A. Krafft, *Phys. Rev. Lett.* **112**, 074801 (2014), URL <http://link.aps.org/doi/10.1103/PhysRevLett.112.074801>.
- [16] J. D. Bjorken and S. D. Drell, *Relativistic Quantum Mechanics* (McGraw-Hill Book Co., 1964), p. 131.
- [17] J. J. Sakurai, *Advanced Quantum Mechanics* (Addison-Wesley Publishing Co., 1967), p. 138, 228-229.
- [18] C. Itzykson and J.-B. Zuber, *Quantum Field Theory* (McGraw-Hill International Book Co., 1980), p. 229.
- [19] M. Boca, C. Stoica, A. Dumitriu, and V. Florescu, *Journal of Physics: Conference Series* **594**, 012014 (2015), URL <http://stacks.iop.org/1742-6596/594/i=1/a=012014>.
- [20] R. Hajima and M. Fujiwara, *Phys. Rev. Accel. Beams* **19**, 020702 (2016), URL <http://link.aps.org/doi/10.1103/PhysRevAccelBeams.19.020702>.
- [21] R. Coisson, *Phys. Rev. A* **20**, 524 (1979), URL <http://link.aps.org/doi/10.1103/PhysRevA.20.524>.
- [22] G. A. Krafft, *Phys. Rev. Lett.* **92**, 204802 (2004), URL <http://link.aps.org/doi/10.1103/PhysRevLett.92.204802>.
- [23] M. A. Stroschio, *Phys. Rev. A* **29**, 1691 (1984), URL <http://link.aps.org/doi/10.1103/PhysRevA.29.1691>.
- [24] M. E. Peskin and D. V. Schroeder, *An Introduction to Quantum Field Theory* (Addison-Wesley Publishing Co., 1995), p. 159-163.
- [25] K.-J. Kim, *American Institute of Physics Conference Proceedings* p. 565 (1989).
- [26] C. Harvey, M. Marklund, and A. R. Holkundkar, *Phys. Rev. Accel. Beams* **19**, 094701 (2016), URL <http://link.aps.org/doi/10.1103/PhysRevAccelBeams.19.094701>.
- [27] P. Chen, G. Horton-Smith, T. Ohgaki, A. W. Weidemann, and K. Yokoya, *Nuclear Instruments and Methods in Physics Research Section A: Accelerators, Spectrometers, Detectors and Associated Equipment* **355**, 107 (1995), URL <http://www.sciencedirect.com/science/article/pii/S0168900294011869>.
- [28] *The python programming language*, URL <http://www.python.org>.
- [29] URL <http://www.scipy.org>.
- [30] URL <http://nines.cs.kuleuven.be/software/QUADPACK>.
- [31] K. Arumugam, A. Godunov, D. Ranjan, B. Terzić, and M. Zubair, *42nd International Conference on Parallel Processing* p. 486 (2013), URL <http://ieeexplore.ieee.org/document/6687383/>.

- [32] K. Arumugam, A. Godunov, D. Ranjan, B. Terzić, and M. Zubair, 20th Annual International Conference on High Performance Computing p. 169 (2013), URL <http://ieeexplore.ieee.org/document/6799120/>.
- [33] W. Graves, W. Brown, F. Kaertner, and D. Moncton, Nuclear Instruments and Methods in Physics Research Section A: Accelerators, Spectrometers, Detectors and Associated Equipment **608**, S103 (2009), ISSN 0168-9002, compton sources for X-rays: Physics and applications, URL <http://www.sciencedirect.com/science/article/pii/S0168900209009802>.
- [34] A. Michalke, Ph.D. thesis, Bergische Universität Gesamthochschule Wuppertal (1993).
- [35] A. Arnold and J. Teichert, Phys. Rev. ST Accel. Beams **14**, 024801 (2011), URL <http://link.aps.org/doi/10.1103/PhysRevSTAB.14.024801>.
- [36] J. Delayen, Proceedings of LINAC2012 p. 758 (2012), URL <https://accelconf.web.cern.ch/AccelConf/LINAC2012/papers/th1a03.pdf>.
- [37] C. S. Hopper, Ph.D. thesis, Old Dominion University (2015).
- [38] C. S. Hopper and J. R. Delayen, Phys. Rev. ST Accel. Beams **16**, 102001 (2013), URL <http://link.aps.org/doi/10.1103/PhysRevSTAB.16.102001>.
- [39] C. Hopper, J. Delayen, and H. Park, pp. 744–746 (2015), URL <http://srf2015.vrws.de/papers/tupb071.pdf>.
- [40] H. Park, C. S. Hopper, and J. R. Delayen, Proceedings of LINAC2014 p. 385 (2014), URL <http://accelconf.web.cern.ch/AccelConf/LINAC2014/papers/mopp138.pdf>.
- [41] *Poisson superfish* (2012), URL [http://laacg1.lanl.gov/laacg/services/download\\_sf.phtml](http://laacg1.lanl.gov/laacg/services/download_sf.phtml).
- [42] *Computer simulation technology website*, URL <http://www.cst.com>.
- [43] J. Qiang, S. Lidia, R. D. Ryne, and C. Limborg-Deprey, Phys. Rev. ST Accel. Beams **9**, 044204 (2006), URL <http://link.aps.org/doi/10.1103/PhysRevSTAB.9.044204>.
- [44] M. Borland, Tech. Rep., Argonne National Lab (2000), URL <http://nines.cs.kuleuven.be/software/QUADPACK>.
- [45] K. Deitrick, Ph.D. thesis, Old Dominion University (2016).
- [46] G. E. Stedman and D. M. Pooke, Phys. Rev. D **26**, 2172 (1982), URL <http://link.aps.org/doi/10.1103/PhysRevD.26.2172>.
- [47] J. M. Jauch and F. Rohrlich, *The Theory of Photons and Electrons* (Addison-Wesley Publishing Co., 1955), p. 234.
- [48] R. P. Feynman, *The Theory of Fundamental Processes* (Benjamin/Cummings Publishing Company, 1961), p. 129-130.
- [49] J. D. Jackson, *Classical Electrodynamics, 2nd Edition* (John Wiley and Sons, 1975), p. 682.
- [50] J. D. Jackson, *Classical Electrodynamics, 3rd Edition* (John Wiley and Sons, 1999), p. 697.
- [51] V. B. Berestetskii, E. M. Lifshitz, and L. P. Pitaevskii, *Quantum Electrodynamics, Course of Theoretical Physics, 2nd Edition* (Pergamon Press, 1982), p. 356.